PAPER Nr.:13

THREE-DIMENSIONAL VISCOUS ROTOR FLOW CALCULATIONS USING BOUNDARY-LAYER EQUATIONS

BY

CHING S. CHEN
NASA AMES RESEARCH CENTER
MOFFETT FIELD, CALIFORNIA, USA

JOHN O. BRIDGEMAN
WOODSIDE SUMMIT GROUP, INC.
MOUNTAIN VIEW, CALIFORNIA, USA

FIFTEENTH EUROPEAN ROTORCRAFT FORUM

SEPTEMBER 12 - 15, 1989 AMSTERDAM

Abstract

A three-dimensional viscous-inviscid interaction analysis has been developed to predict the performance of rotors in hover and forward flight at subsonic and transonic tip speeds. The analysis solves the full-potential and boundary-layer equations by finite-difference numerical procedures. Calculations were made for several different model rotor configurations in hover and forward flight at subsonic and transonic tip speeds. The results were compared with predictions from a two-dimensional integral method and with experimental data. The comparisons show good agreement between test data and predictions.

Nomenclature

a_∞ = ambient speed of sound
c = root chord length
C_p = nondimensional specific heat coefficient
h = nondimensional time step in full-potential method
H = nondimensional total enthalpy
J = grid Jacobian
M_1, M_2 = Mach number upstream and downstream of a shock
p_∞ = ambient pressure
p = nondimensional pressure
R = perfect gas constant
s_1, s_2 = entropy upstream and downstream of a shock
T = nondimensional temperature
u_e = nondimensional tangential velocity on body surface in full-potentail method
u,v,w = nondimensional velocities in x,y,z directions
U,V,W = contravariant velocities
V_δ = transpiration velocity
x,y,z = rotor blade coordinate system; x-parallel to blade chord, y-normal to blade surface, z-parallel to blade radius
β = $p_\infty / (\rho_\infty a_\infty^2)$
μ = nondimensional viscosity, the sum of molecular and eddy viscosities.
ρ = nondimensional density
ρ_e = nondimensional density on body surface in full-potentail method
ρ_i = nondimensional isentropic density
ρ_∞ = ambient density
δ^* = displacement thickness

t = nondimensional time in full-potential method

γ = ratio of specific heats

ϕ = velocity potential

Ω^* = tip Mach number/aspect ratio

Δs = entropy difference

∂d = distance along body surface

ξ, η, ζ = transformed rotor blade coordinate system; ξ-parallel to blade chord, η-normal to blade surface, ζ-parallel to blade radius

τ = shear stress

ω = relaxation parameter in boundary-layer method

Superscript

n = time step for full-potential method

1. Introduction

The ability to accurately predict performance is important in the design of rotorcraft. Advancements in computational fluid dynamics now allow some complex rotor performance predictions to be performed routinely to help guide engineers in the design process. There are several different levels of complexity in the methods available for this purpose. Their use depends upon the flow field information needed by the designer. The more complex methods provide more detailed information about the flow field but in general are more expensive computationally.

These prediction methods range in complexity from simple lifting-line theory, to lifting-surface theory, to sophisticated finite difference methods (small-disturbance, full-potential, Euler, and Navier-Stokes). Only the Navier-Stokes method can predict viscous drag directly. However, this method requires large computer memory and long CPU times. The other methods rely on either (1) two-dimensional airfoil tables or (2) approximate methods to predict the viscous drag. There are several problems with the first approach. First, two-dimensional airfoil data does not model the highly three-dimensional flow behavior at the tip region due to complex tip shapes or transonic flow unsteadiness in forward flight. Second, it does not take the variations in Reynolds number or the rotational effects of the blade into account. Third, for airfoils yet to be tested, the results may be dubious.

Adopting the second approach, Bridgeman et al [1] incorporated a two-dimensional integral boundary-layer method, the Nash-MacDonald scheme [2], into a full-potential finite-difference method to predict the viscous drag directly. The advantages of this approach are that it is fast-running, easy to implement and fairly robust for attached boundary-layer flows. The disadvantages are that it cannot handle three-dimensional flow phenomena at the blade tip and for flows with separation the results are less certain. One possibility for solving these problems is the incorporation of three-dimensional boundary-layer equations into the analysis.

In the present study, a three-dimensional boundary-layer finite-difference method is coupled with a full-potential finite-difference method to form a viscous-inviscid interaction analysis. The boundary-layer method [3], BL3D, was originally developed by Van Dalsem and Steger for applications in fixed-wing flows. The full-potential method was developed by Strawn et al [4] for inviscid rotor flows. The interaction analysis is developed to make rotor performance predictions efficiently for general rotor configurations without the above mentioned problems.

The accuracy of BL3D was first evaluated by simulating flows over a flat plate and two dimensional airfoils. The comparison with theoretical and experimental data shows good accuracy of the method. The interaction analysis was then used to calculate nonlifting model rotor flows in hover and forward flight. The agreement between predictions and test data demonstrate the capability of the analysis.

The computational efforts for rotor flows have been concentrated on nonlifting flows for both hover and forward flight. This is because: (1) it is not possible to measure viscous drag directly in lifting flows and (2) the influences due to rotor wake can be minimized. In lifting rotor flows, the wake shed by the blades plays a very important role in the performance prediction. Viscous drag is only around twenty to thirty percent of the total drag. A slightly different wake geometry could alter the pressure drag by ten percent. In addition, wake geometry prediction is still in its development stage, especially for advanced rotor configurations.

2. Viscous Formulation - Boundary-Layer Method

In the boundary-layer method the unsteady, three-dimensional, compressible boundary-layer equations are solved in a rotating reference frame. A general x,y,z to $\xi(x, z)$, $\eta(x, y, z)$, $\zeta(x, z)$ coordinate transformation is used to avoid a complex similarity transformation. The two sets of coordinate systems are shown in Fig.1.

2.1 Boundary-Layer Equations

Neglecting surface curvature, the nondimensional boundary-layer equations for a perfect gas can be written in $\xi(x, z), \eta(x, y, z), \zeta(x, z)$ coordinates as [3]

x-momentum equation

$$\rho u_t + \rho(Uu_\xi + Vu_\eta + Wu_\zeta - 2w\Omega^* - x(\Omega^*)^2)$$
$$= -\beta(p_\xi \xi_x + p_\zeta \zeta_x) + (\mu u_\eta \eta_y)_\eta \eta_y \tag{1}$$

z-momentum equation

$$\rho w_t + \rho(Uw_\xi + Vw_\eta + Ww_\zeta + 2u\Omega^* - z(\Omega^*)^2)$$
$$= -\beta(p_\xi \xi_z + p_\zeta \zeta_z) + (\mu w_\eta \eta_y)_\eta \eta_y \tag{2}$$

perfect gas relation

$$p = \rho T \tag{3}$$

energy equation (H=total enthalpy)

$$H \equiv C_p T + \frac{1}{2}(u^2 + v^2 + w^2) = \text{CONSTANT} \tag{4}$$

continuity equation

$$\rho_t + (\rho u)_\xi \xi_x + (\rho u)_\eta \eta_x + (\rho u)_\zeta \zeta_x + (\rho v)_\eta \eta_y$$
$$+ (\rho w)_\xi \xi_z + (\rho w)_\eta \eta_z + (\rho w)_\zeta \zeta_z = 0 \tag{5}$$

and

$$\begin{bmatrix} U \\ V \\ W \end{bmatrix} = \begin{bmatrix} \xi_t + \xi_x u + \xi_z w \\ \eta_t + \eta_x u + \eta_y v + \eta_z w \\ \zeta_t + \zeta_x u + \zeta_z w \end{bmatrix} \tag{6}$$

where U, V, and W are unscaled contravariant velocities, $\Omega^* = $ tip Mach number/aspect ratio, $\beta = p_\infty / (\rho_\infty a_\infty^2)$, and a_∞ is the ambient speed of sound.

Viscosity, pressure, temperature, and density are nondimensionalized by the ambient values. The velocities u and w are nondimensionalized by the ambient speed of sound. The coordinates x and z are nondimensionalized by a characteristic length, typically the chord length at the blade root. The v and y variables are nondimensionalized by the same quantities divided by $\sqrt{Re_\infty}$. For turbulent flows, the viscosity is the sum of the molecular and eddy viscosities. The eddy viscosity is evaluated by Cebeci's two-layer algebraic turbulence model [5].

Of note are the four terms $2w\Omega^*$, $x(\Omega^*)^2$, $2u\Omega^*$, and $z(\Omega^*)^2$ in the x- and z-momentum equations. They represent Coriolis and centrifugal forces in the boundary-layer induced by the rotation of the blade.

2.2 Solution Algorithm

A relaxation algorithm [3] is used to solve the boundary-layer equations. The advantages of using relaxation over space marching are that it is easier to implement and simpler boundary conditions can be specified. For example, it would be very difficult to specify the flow quantities at the tip of the blade as required by a space marching algorithm. In a relaxation algorithm, a zero- or first-order boundary condition can be used with local grid mesh refinement to minimize the impact on the final results [3].

The pressure terms in Eqs.(1) and (2) are treated as known functions. The boundary-layer equations are weakly coupled and can be solved sequentially at each time (or iteration) step. As a result, a semi-implicit scheme is used at each time step. The time derivatives are approximated with a first-order-accurate forward-difference operator. The space derivatives in the direction normal to the body are approximated with a second-order-accurate central-difference operator and second-order-accurate backward-difference operators are used for the other two directions.

The FLARE approximation [6] is employed in the reversed flow regions in the streamwise direction. That is, the streamwise convection term is dropped out if the streamwise velocity is negative. This is justified by arguing that the streamwise velocity in the reversed flow regions is small in magnitude, usually less than ten percent of the maximum velocity found in the viscous region [6]. In the continuity equation, the derivatives in the ξ and ζ directions are approximated with second order central-difference operators, and trapezoidal-rule integration is used in the η direction to calculate the v velocity.

The typical grid mesh [7] used by BL3D for the calculations in this paper is 40 points in the chordwise direction, 16 in the spanwise direction, and 50 in the direction normal to the blade surface. The upper and lower surfaces of the blade are calculated separately. The computation starts a small distance away from the stagnation point at the leading edge. The flow velocities at the initial plane are assumed to have known values, and are obtained by solving the Falkner-Skan similarity equations [8]. At each time step the computation starts from the initial plane, sweeps through the grid mesh and ends at the trailing edge. A first-order boundary condition is used at the trailing edge. The wake was not included in the calculations made to date.

The solution algorithm for flows with a strong shock or a major separation is not very robust. Our experience shows that the boundary-layer method is very sensitive to the large adverse pressure gradient at the shock or the trailing edge. In calculating flows with a strong shock, typically when the tip Mach number is greater than 0.92, the shock has to be smoothed to prevent the computation from diverging. However, since rotors are seldom operated with tip Mach numbers this large, this problem has little practical significance. The trailing edge stagnation point is another persistent problem. An O-grid is used in the full-potential method, and it seems that the adverse pressure gradient predicted is too large. Our experience shows that pressure smoothing, along with a transpiration flux limiter, which prevents the excessive boundary-layer growth from destabilizing the potential flow, has to be applied at the trailing edge, even in flows with low tip Mach number, to prevent the solutions from diverging. In all calculations, fully turbulent flow was assumed.

3. Inviscid Formulation - Full Potential Method

The inviscid flow is assumed to be isentropic, inviscid, and irrotational. These assumptions are suitable for a wide range of transonic flows. For flows with a strong shock, a nonisentropic correction is added to the formulation to account for the entropy produced at the shock.

3.1 Equations

The unsteady, three-dimensional, full-potential equation in strong conservation form is written in generalized coordinates as [4]

$$\frac{\partial}{\partial \tau}\left(\frac{\rho}{J}\right) + \frac{\partial}{\partial \xi}\left(\frac{\rho U}{J}\right) + \frac{\partial}{\partial \eta}\left(\frac{\rho V}{J}\right) + \frac{\partial}{\partial \zeta}\left(\frac{\rho W}{J}\right) = 0 \qquad (7)$$

with density given by

$$\rho = \{1 + \frac{\gamma-1}{2}[-2\phi_t - (U+\xi_t)\phi_\xi - (V+\eta_t)\phi_\eta - (W+\zeta_t)\phi_\zeta]\}^{\frac{1}{\gamma-1}} \qquad (8)$$

where

$$\begin{aligned} U &= \xi_t + A_1\phi_\xi + A_4\phi_\eta + A_5\phi_\zeta \\ V &= \eta_t + A_4\phi_\xi + A_2\phi_\eta + A_6\phi_\zeta \\ W &= \zeta_t + A_5\phi_\xi + A_6\phi_\eta + A_3\phi_\zeta \end{aligned} \qquad (9)$$

and

$$\begin{aligned} A_1 &= \xi_x^2 + \xi_y^2 + \xi_z^2 \\ A_2 &= \eta_x^2 + \eta_y^2 + \eta_z^2 \\ A_3 &= \zeta_x^2 + \zeta_y^2 + \zeta_z^2 \\ A_4 &= \xi_x\eta_x + \xi_y\eta_y + \xi_z\eta_z \\ A_5 &= \xi_x\zeta_x + \xi_y\zeta_y + \xi_z\zeta_z \\ A_6 &= \eta_x\zeta_x + \eta_y\zeta_y + \eta_z\zeta_z \end{aligned} \qquad (10)$$

In the above equations, ρ is the fluid density, U,V, and W are contravariant velocities, and J is the grid Jacobian. The velocity potential is given by ϕ, and the generalized coordinates are ξ, η, ζ, and t. All velocities are normalized by the ambient speed of sound, a_∞, distances by the root chord length c, and time by the combination (c/a_∞). Density is normalized by the free-stream value ρ_∞.

3.2 Density Correction for Nonisentropic Flow

A nonisentropic Bernoulli relation is used for density [4],

$$\rho = \rho_i e^{-\Delta s / R} \qquad (11)$$

where ρ_i is the isentropic density given by Eq.(8).

The entropy correction to the density is made at the half-point just downstream of the shock. The Rankine-Hugoniot equation is used to calculate the entropy change across the shock [9].

$$\frac{\Delta s}{R} = \frac{s_2 - s_1}{R} = \frac{\gamma}{\gamma-1}\ln\left[\frac{2}{(\gamma+1)M_1^2} + \frac{\gamma-1}{\gamma+1}\right] + \frac{1}{\gamma-1}\ln\left[\frac{2\gamma}{(\gamma+1)}M_1^2 - \frac{\gamma-1}{\gamma+1}\right] \qquad (12)$$

where R is the perfect gas constant, and the subscripts 1 and 2 denote the upstream and downstream conditions of a shock respectively.

3.3 Solution Algorithm

Eq.(7) is solved by using first-order backward differencing in time and second-order central differencing in space. The temporal density derivative is locally linearized about the old time levels in a manner that preserves the conservative form [10]. The resulting equation is approximately factored into ξ, η, and ζ operators.

$$L_\xi L_\eta L_\zeta (\phi^{n+1} - \phi^n) = \mathrm{RHS} \tag{13}$$

where

$$L_\xi = \left[I + hU^n \delta_\xi - \frac{h^2}{\hat{\beta}^n} \delta_\xi (\beta A_1)^n \delta_\xi \right]$$

$$L_\eta = \left[I + hV^n \delta_\eta - \frac{h^2}{\hat{\beta}^n} \delta_\eta (\beta A_2)^n \delta_\eta \right]$$

$$L_\zeta = \left[I + hW^n \delta_\zeta - \frac{h^2}{\hat{\beta}^n} \delta_\zeta (\beta A_3)^n \delta_\zeta \right] \tag{14}$$

and

$$\mathrm{RHS} = \frac{h^2}{\hat{\beta}^n} \left[\delta_\xi (\beta U)^n + \delta_\eta (\beta V)^n + \delta_\zeta (\beta W)^n - R \right] + C \tag{15}$$

which represents central difference operators in space. The term C is given by

$$C = \left[I + h \frac{\hat{\beta}^{n-1}}{\hat{\beta}^n} \left(U^{n-1} \delta_\xi + V^{n-1} \delta_\eta + W^{n-1} \delta_\zeta \right) \right] \left(\phi^n - \phi^{n-1} \right)$$
$$+ \frac{\hat{\beta}^{n-1}}{\hat{\beta}^n} \left(\phi^n - 2\phi^{n-1} + \phi^{n-2} \right) + \frac{h}{\hat{\beta}^n} \left(\beta^n - \beta^{n-1} \right) \tag{16}$$

The bracketed term in Eq.(16) represents the temporal conservation in the algorithm. In the above equations, h is the time step, $\hat{\beta} = \rho^{2-\gamma} / J$, and $\hat{\rho} = \rho / J$. The superscript represents the time step.

A steady state ADI relaxation algorithm can be obtained from Eq.(13) by omitting the unsteady C term on the right-hand side of the equation, adding temporal dissipation in the ξ direction, and allowing for a time-stepping sequence for accelerated convergence.

The basic grid system is composed of a series of parallel chordwise O-grids. Body motion is incorporated by assigning an appropriate coordinate velocity $(\xi_\tau, \eta_\tau, \zeta_\tau)$ to each grid point. The coordinate velocity is defined with respect to an inertial coordinate frame. The coordinate velocity can be translational, rotational, or the combination.

The angle-of-attack conditions on the blade surface (including inflow-angles induced by the rotor wake) are simulated by a transpiration velocity condition. At the outer radial boundary of the O-grid, a nonreflection boundary condition is used to prevent the accumulation of numerical disturbances. Typical grid size for the inviscid calculations in this paper is 80 points in the chordwise direction, 25 in the spanwise direction, and 25 in the direction normal to the rotor surface. The finite difference grid extends approximately two chords outward from the rotor tip in the spanwise direction. The outer radial boundary of the O-grid is about five chords from the blade surface. Variable time steps are used for the steady flows, such as hover, to accelerate convergence.

4. Coupling of Viscous and Inviscid Solutions

To obtain a meaningful solution, the viscous-inviscid interaction must allow each flow to influence the other. The classical way of introducing viscous effects into an inviscid flow is to add displacement thickness to the body surface. In doing so the geometry of the body and therefore the grids need to be recomputed after each iteration. This is computationally costly. A more efficient and robust alternative is to impose a transpiration velocity at the body surface, as first suggested by Lighthill [11].

4.1 Viscous to Inviscid Interaction

In this approach the original flow tangency condition in the inviscid flow is modified by enforcing a normal velocity component on

the body. A flowchart depicting the viscous-inviscid interaction process is shown in Fig.2. The normal velocity component (i.e. the transpiration velocity) deflects the inviscid flow from the body surface thus simulating the displacement of the inviscid flow due to the momentum defect in the boundary-layer. The transpiration velocity due to the boundary-layer is given by

$$V_\delta = \frac{1}{\rho_e}\frac{\partial(\rho_e u_e \delta^*)}{\partial d} \qquad (17)$$

where ρ_e, u_e are inviscid density and tangential velocity on the body surface, δ^* is the displacement thickness, and d is the distance along the body surface.

Depending upon the application, it is sometimes not necessary to recompute viscous flow after each inviscid iteration. This happens because the inviscid flow does not change much between iterations. In order to speed up the convergence, the ratio of inviscid to viscous iterations was set to five for all hover calculations. For forward flight calculations, however, the ratio was set to one since the computation was unsteady.

4.2 Inviscid to Viscous Interaction: Direct and Inverse Modes

Depending upon the flow conditions, the inviscid solution can be incorporated into the boundary-layer equations in one of two ways. If the flow is fully attached, i.e., no separation, the boundary-layer equations can be solved directly with pressures provided by the full-potential method. This direct mode solution process is quite straightforward. If the flow separates, however, the direct mode cannot be used because: (1) there is a singularity at the separation point and (2) flow reversal prohibits marching the solution in the direction of the external flow unless the convection terms in the momentum equations are altered [6]. An inverse mode is needed in this case. In the inverse mode, wall shear stress and wake centerline velocity are treated as the forcing functions in the momentum equations, and pressure becomes part of the solution [7].

To solve the boundary-layer equations in the inverse mode, the algorithm needs to be modified so that the inverse forcing functions can be specified. This is achieved by replacing the pressure terms in the momentum equations with the inverse forcing functions. These relations are obtained by applying the momentum equations on the body surface or the wake centerline. For example, applying the x-momentum equation on the body surface yields

$$\beta(p_\xi \xi_x + p_\zeta \zeta_x)$$
$$= \rho(2w\Omega^* + x(\Omega^*)^2) + [(\mu u_\eta \eta_y)_\eta \eta_y]_{wall} \qquad (18)$$

These expressions allow the pressure terms to be replaced by the inverse forcing functions. After the boundary-layer equations are solved in the inverse mode at each iteration, the pressure is calculated by assuming the fluid is an isentropic perfect gas.

A shear stress distribution is first assumed for the proposed separated regions at the beginning of the computation and is then updated by the following equation,

$$\tau^{n+1} = \tau^n + \omega(p_{viscous} - p_{inviscid}) \qquad (19)$$

This update is continued until the pressure predicted by the viscous method matches that of the inviscid method. ω is a relaxation parameter; a value of 0.1 was used in most of the calculations.

Currently, the inverse mode can be applied only in one direction, usually the streamwise direction. This restriction is due to the fact that in the inverse mode the wall shear stress or the wake center line velocity is updated by the inviscid and viscous pressure difference. If the inverse mode is applied in both streamwise and spanwise directions then the pressure will have to be calculated in these two directions during the same iteration. The pressure calculated in the spanwise direction will not be the same as that calculated in the chordwise direction. We then face a question of which pressure, chordwise or spanwise, should be used to update the inverse forcing function as described in Eq.(19). Further study is needed to insure that this double updating process would not cause convergence problems before implementation.

5. Results and Discussion

5.1 Flat Plate Flows

Prior to running the coupled viscous-inviscid interaction code, an attempt was made to validate the accuracy of the boundary-layer method, BL3D, by itself. This was accomplished by computing both laminar and turbulent flows over a flat plate. The Reynolds number for the laminar flow was 10^5. The computed local friction coefficients are compared with the analytical results derived from a Blasius solution [12] in Fig.3. The comparison is excellent. For the turbulent flow, the

Reynolds number was 10^6. The computed local friction coefficients are compared with experimental data [12] in Fig.4. BL3D consistently underpredicts the friction coefficient by about ten percent. This underprediction is believed to be due to Cebeci's turbulence model used.

5.2 Two-Dimensional Airfoil Flows

The viscous-inviscid interaction analysis was then used to compute nonlifting, two-dimensional airfoil flows with a NACA 0012 airfoil. Flows with two different Reynolds numbers, 10^6 and 10^7, and a Mach number range of 0.3 to 0.8 were computed. In these computations the aspect ratio of the blade was set very large, 10000, such that a few chords away from the tip the flow is essencially two dimensional, and the flows were assumed fully turbulent. The computed drag coefficients are compared with experimental data [13] for the lower Reynolds number flow, 10^6, in Fig.5. The comparison is very good as the computed drag coefficients are well within the test band. The analysis predicts a drag rise Mach number of 0.77, which is also confirmed by the experimental data.

A similar comparison is made for the higher Reynolds number flow in Fig.6. The analysis slightly underpredicts the drag coefficients. This discrepancy is believed to be due to Cebeci's turbulence model employed. But since only one turbulence model is used in the analysis, no definite conclusion can be drawn here. The analysis again predicts a drag rise Mach number of 0.77, which is consistent with the experimental data [13]. Note that the analysis predicts higher magnitude drag coefficients for lower Reynolds number flow as anticipated.

The solutions of version one of the full-potential code [1] had a large pressure drag tare, about eighty counts. Theoretically, an object should experience no drag if the flow is inviscid and subsonic. The numerical algrithm had been improved to reduce the tare value as described in Ref. [4]. A small tare value still exists after the improvement. This numerical tare value is small, less than five percent for subsonic flows when compared with Euler method [4]. Its value is less certain in the transonic region because it is mixed with wave drag. All the results in this paper did not exclude the tare value.

5.3 Nonlifting Hovering Rotor Flows

The analysis was used to compute the nonlifting hovering flow for a two-bladed model rotor system. The blade is untwisted and rectangular, with a NACA 0012 section and an aspect ratio of 13.71.

Fig.7 shows the comparison of torques calculated by the present analysis with that of test data for a tip Mach number range of 0.3 to 0.925. The comparison is excellent. Also plotted in this figure are torques calculated using the two-dimensional integral boundary-layer method as described in Ref. [4]. This integral boundary-layer method underpredicts the torque in the higher tip Mach number region (greater than 0.7). Fully turbulent flow was assumed in the calculations of both methods.

To validate the current approach for advanced rotor configurations, the analysis was used to calculate the flow of another nonlifting hovering rotor system. This system consisted of two swept, tapered tip blades with variable airfoil thickness. Details of this rotor can be found in Ref. [4]. The torques calculated are compared with those calculated by the integral boundary-layer method and with the test data as shown in Fig.8. The comparison shows that the present method consistently overpredicts the torque by about ten to fifteen percent for the range of tip Mach numbers considered. The predictions made by the integral method agree well with the test data in the low tip Mach number region (less than 0.7), but underpredict the values in the high tip Mach number region (greater than 0.7).

To investigate the differences in the torque predictions made by the present method and the integral method, the spanwise variations in the viscous drag coefficients obtained from BL3D and the integral method were compared. Fig.9 shows the comparison for the nonlifting hovering rotor with rectangular blades at a tip Mach number of 0.9. In calculating the viscous drag coefficient, the surface shear component in the outer flow direction was integrated to obtain the drag coefficient. The wave drag due to shock was not included. As shown in Fig.9, BL3D does predict a higher viscous drag coefficient. The difference is very large in the inboard region and becomes significantly smaller near the tip.

The same comparison was made for the nonlifting hovering rotor with swept, tapered tip blades at the same tip Mach number in Fig.10. The viscous drag coefficient difference is not as large in the inboard region, as was the case in the previous comparison, but becomes larger near the tip region. The value of viscous drag coefficient calculated by the integral method drops rapidly at the tip region. This might be caused by the inability of the integral method, which was developed for two-dimensional flows, to handle the highly three-dimensional flow at the tip region generated by the swept, tapered tip.

Comparing the viscous drag coefficients calculated by BL3D for the rectangular and the swept tip blades, one finds that the drag

coefficient drops faster from blade root to tip on the rectangular blade than on the swept tip blade. This is caused by the strength of shock being stronger on the rectangular blade. The reversed flow region is larger, thereby reducing the drag coefficient more.

In order to understand the effects of adding the nonisentropic correction and the viscous-inviscid interaction on the inviscid (full-potential) analysis, pressure coefficient distributions obtained from two sets of different calculations are compared. In set one the pressure coefficient was calculated by the isentropic full-potential analysis alone. In set two the pressure coefficient was calculated by the viscous-inviscid interaction plus the nonisentropic correction. The comparison is made for the nonlifting two-bladed model rotor with rectangular tips in hover, as used in the calculations for Fig.7., over six different spanwise locations, from r/R equals 0.820 (Fig.11a) to 0.998 (Fig.11f). The tip Mach number was 0.925. In the inboard region the flow is subsonic, and the results predicted by set one and two are quite close. Near the tip region the flow is transonic, the shock is much stronger, and the predictions have some significant differences as far as the shock is concerned. In general, using a nonisentropic viscous analysis predicts a weaker shock as well as moving the location of the shock slightly upstream. This not only affects the drag force but also the blade pitching moment which is important in rotor dynamics.

5.4 Nonlifting Rotor Flows in Forward Flight

An important issue to be addressed is the applicability of the current viscous-inviscid interaction approach to the prediction of unsteady flows. To demonstrate this applicability, flow about a nonlifting two-bladed model rotor in forward flight was calculated. The blade is untwisted, rectangular planform and has a NACA 0012 section and an aspect ratio of 7.125. Figs. 12 and 13 show comparisons of measured surface pressures [14] with predictions for a tip Mach number of $M_T = 0.763$, an advance ratio of $\mu = 0.246$ and at two radii (r/R=0.876 and r/R=0.946, respectively). The unsteady solution is shown for azimuthal intervals of 30°. The analysis predicts a slightly weaker shock at 60° and 90° of azimuthal angles. The strength of the shock predicted is high at 120°. The shock location predicted at 150° is slightly more upstream. In spite of the above mentioned discrepancies, the analysis does demonstrate that it is able to predict the blade surface pressure distribution of an advancing rotor very well.

6. Conclusions

A viscous-inviscid interaction analysis has been developed to predict the performance of rotor in hover and forward flight. The viscous drag can be calculated directly to include the variations in Reynolds number and the rotational effects of the blade. Flows over flat plate and two-dimensional airfoil flows are first calculated and the results are compared with test data. The comparison shows good accuracy of the numerical procedure. Three nonlifting model rotor flows, two in hover and one in forward flight, are calculated. The comparison of predictions with test data demonstrate that the present analysis is able to make accurate rotor performance predictions efficiently for general rotor configurations.

There are two restrictions in applying this approach to rotor flows. First, it can only handle separation in one direction, either radial or chordwise. If the flow separates in one direction, then flow in the other direction is assumed attached. Second, the approach permits only small amounts of separation. If the separation is large, the solution will diverge. More study is needed in relieving these restrictions.

The pressure drag tare described in the previous section is due to the numerical scheme and grid mesh. Further research is being undertaken by the authors in this area. With the experience gained from nonlifting flow calculations, the next step is to extend the present method to the prediction of lifting flows.

7. References

1. J.O. Bridgeman, R.C. Strawn, and F.X. Caradonna, "An Entropy and Viscosity Corrected Potential Method for Rotor Performance Prediction," The 44th Annual Forum of the American Helicopter Society, Washington, D.C., June, 1988.

2. J.F. Nash and A.G.J. Macdonald, "The Calculation of Momentum Thickness in a Turbulent Boundary-Layer at Mach Numbers up to Unity," Aeronautical Research Council C.P. No. 963, London, 1967.

3. W.R. Van Dalsem and J.L. Steger, "The Efficient Simulation of Separated Three-Dimensional Viscous Flows Using the Boundary-layer Equations," AIAA Paper No. 85-4064, Presented at the AIAA 3rd Applied Aerodynamics Conference, Colorado Springs, Colorado, October, 1985.

4. J.O. Bridgeman, R.C. Strawn, F.X. Caradonna, and C.S. Chen, "Advanced Rotor Computations with A Corrected Potential Method," The 45th Annual Forum of the American Helicopter Society, Boston, Massachusetts., May, 1989.

5. T. Cebeci, "Calculation of Compressible Turbulent Boundary-Layers with Heat and Mass Transfer," AIAA Paper No. 70-741, Presented at the AIAA 3rd Fluid and Plasma Dynamics Conference, Los Angels, California, June, 1970.

6. D.A. Anderson, J.C. Tannehill, and R.H. Pletcher, "Computational Fluid Mechanics and Heat Transfer," Hemisphere Publishing Corporation, New York, 1984.

7. W.R. Van Dalsem, "Simulation of Separated Transonic Airfoil Flow by Finite-Difference Viscous-Inviscid Interaction," Ph. D. Dissertation, Stanford University, Palo Alto, California,1984.

8. F.M. White, "Viscous Fluid Flow," McGraw-Hill Book Company, New York, 1974.

9. A.H. Shapiro, "The Dynamics and Thermodynamics of Compressible Fluid Flow," Volume 1, John Wiley & Sons Inc., New York, 1953.

10. J.O. Bridgeman, J.L. Steger, and F.X. Caradonna, "A Conservative Finite-Difference Algorithm for the Unsteady Transonic Potential Equation in Generalized Coordinates," AIAA Paper No. 82-1388, Presented at the AIAA 9th Atmospheric Flight Mechanics Conference, San Diego, California, August, 1982.

11. M.J. Lighthill, On Displacement Thickness, "Journal of Fluid Mechanics," Vol. 4, 1958, pp. 383-392.

12. H. Schlichting, "Boundary Layer Theory," Seventh Edition, McGrow-Hill Book Company, New York, 1979.

13. W.J. McCroskey, "A Critical Assessment of Wind Tunnel Results for the NACA 0012 Airfoil, AGARD Symposium on Aerodynamic Data Accuracy and Quality: Requirements and Capabilities in Wind Tunnel Testing," September, 1987, AGARD-CP 429, Paper No. 1.

14. F.X. Caradonna, J.L. Lautenschlager, and M.J. Silva, "An Experimental Study of Rotor Blade-Vortex Interactions," AIAA Paper No. 88-0045.

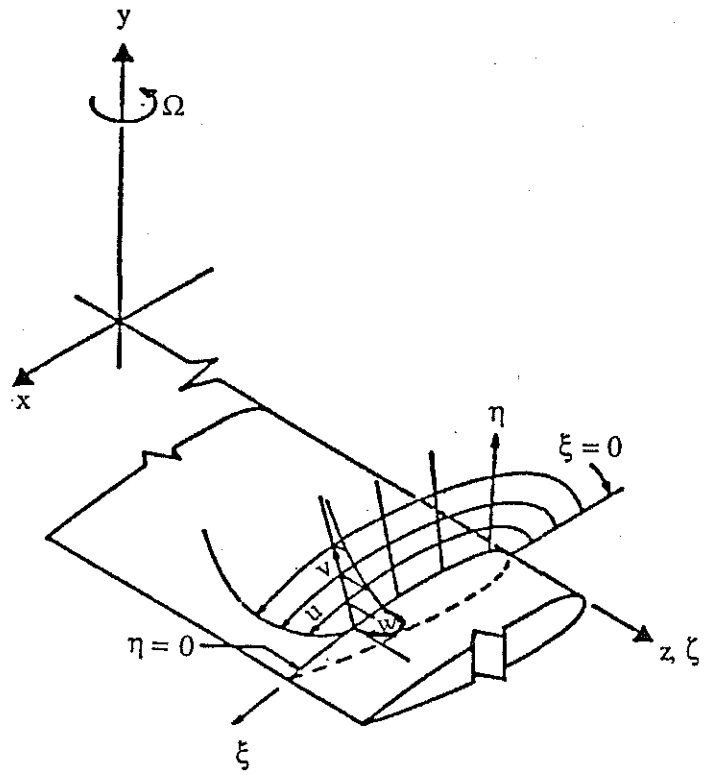

Fig. 1: Coordinate systems for a rotating reference frame.

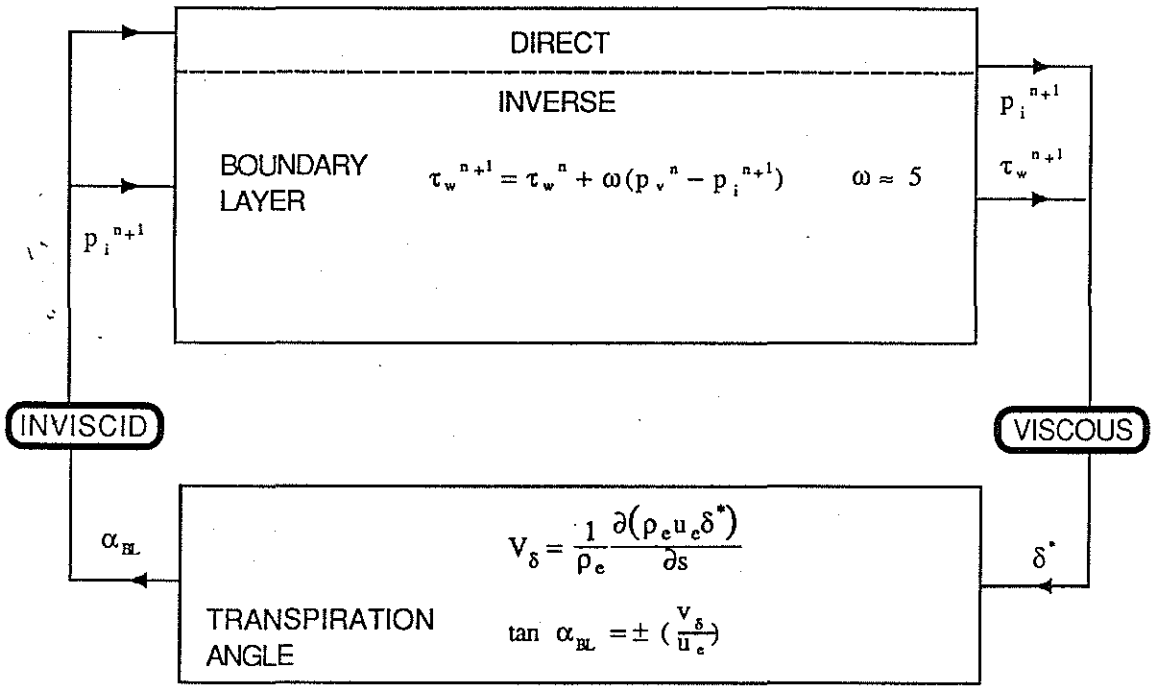

Fig. 2: Flowchart for viscous-inviscid interaction process.

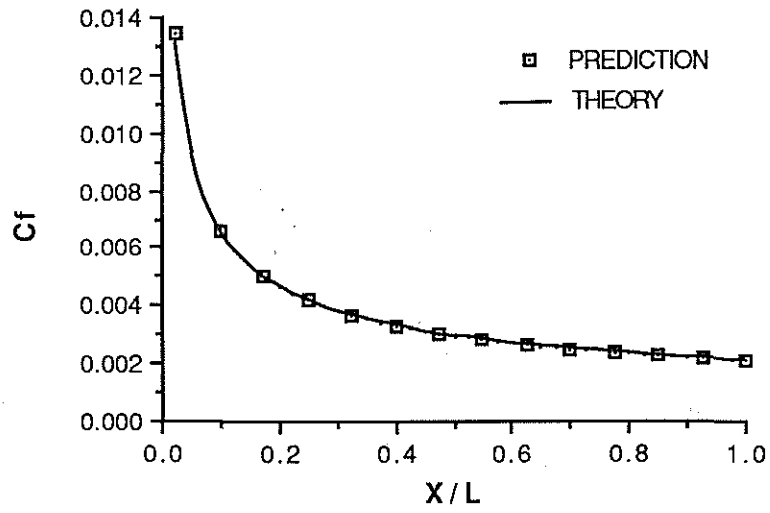

Fig. 3: Comparison of computed local friction coefficients and analytical solution for laminar flow over a flat plate.

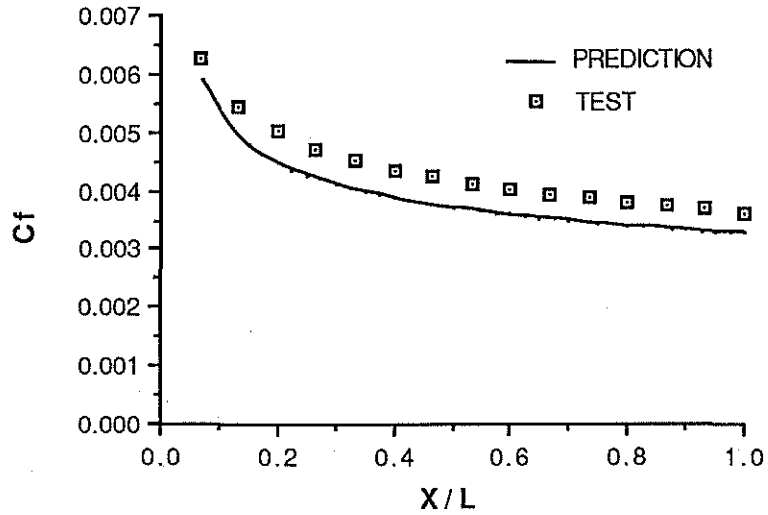

Fig. 4: Comparison of computed local friction coefficients and experimental data for turbulent flow over a flat plate.

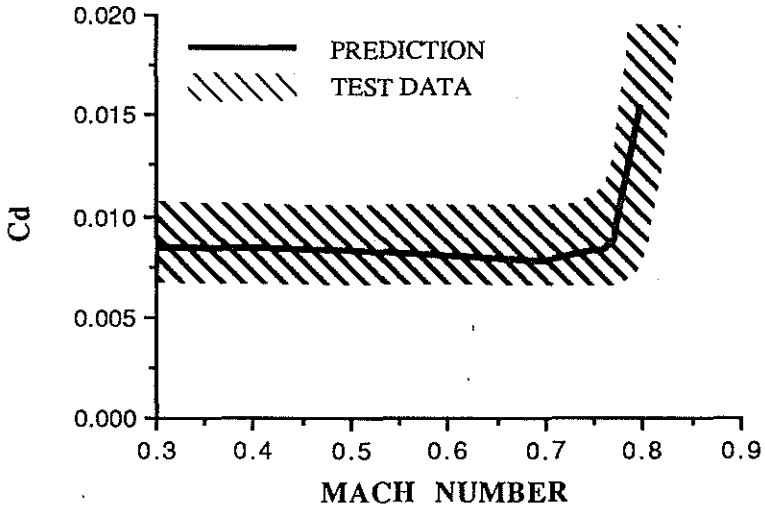

Fig. 5: Comparison of computed drag coefficients and the experimental data for two-dimensional NACA 0012 airfoil flow with a Reynolds number of 10^6.

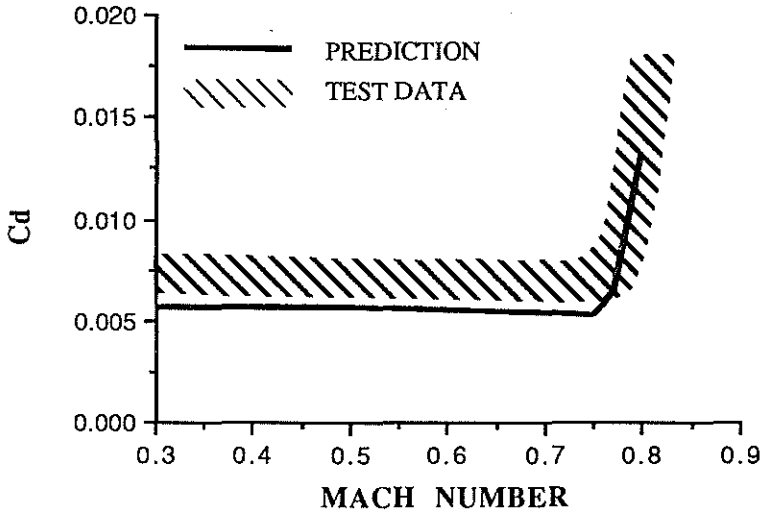

Fig. 6: Comparison of computed drag coefficients and the experimental data for two-dimensional NACA 0012 airfoil flow with a Reynolds number of 10^7.

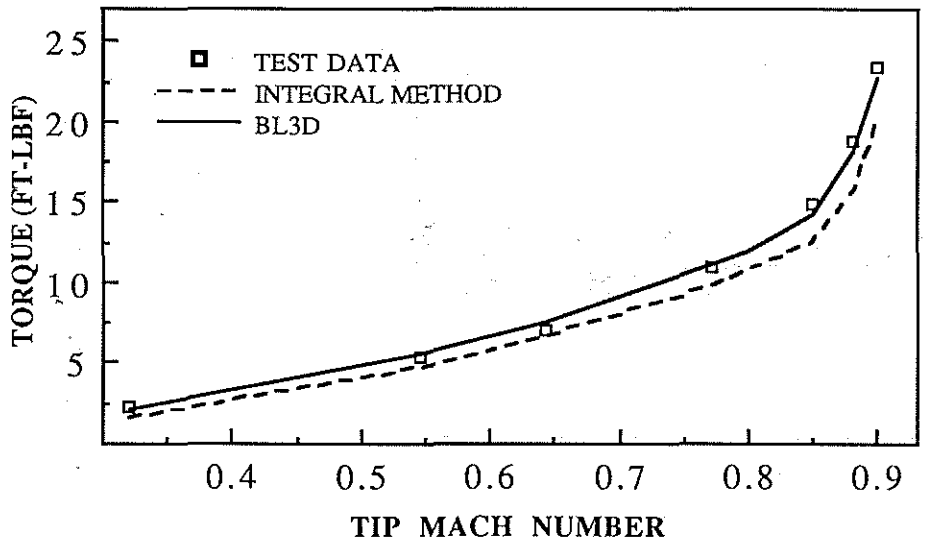

Fig. 7: Comparison of computed torques with test data for the hovering rotor with rectangular blades.

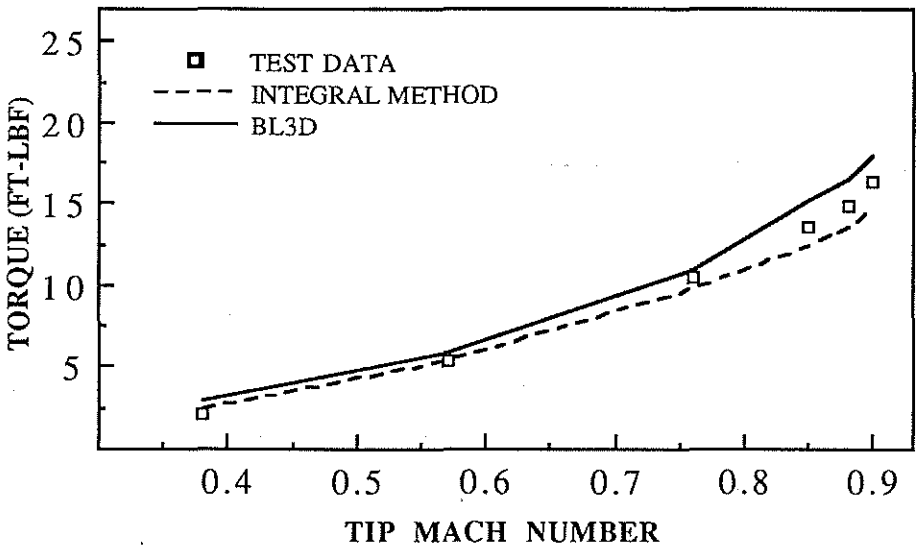

Fig. 8: Comparison of computed torques with test data for the hovering rotor with swept tip blades.

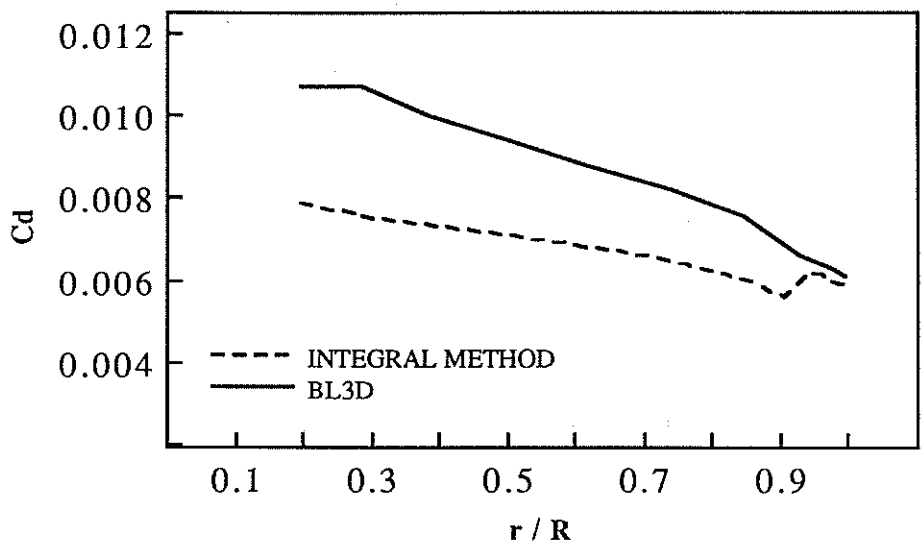

Fig. 9: Comparison of spanwise drag coefficients computed by BL3D and the integral method for the nonlifting hovering rotor with rectangular blades at a tip Mach number of 0.9.

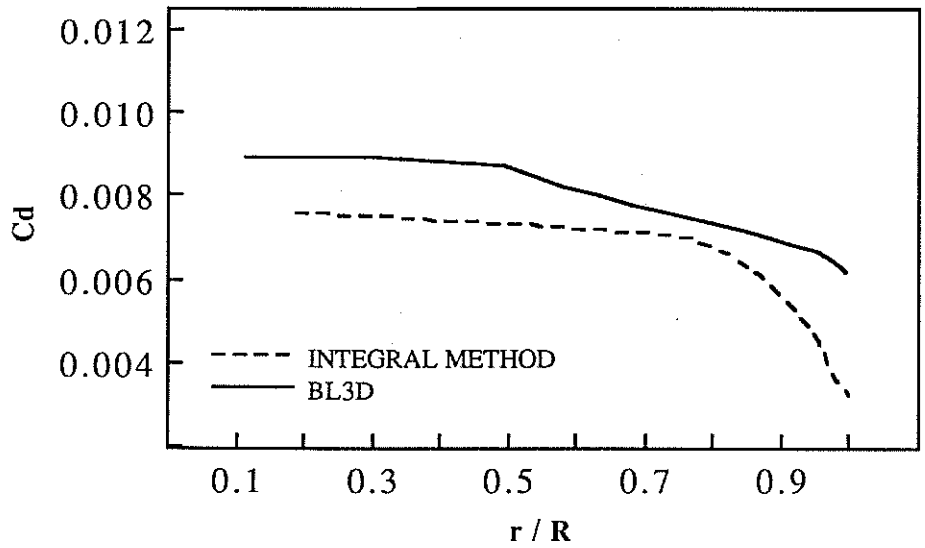

Fig. 10: Comparison of spanwise drag coefficients computed by BL3D and the integral method for the nonlifting hovering rotor with swept tip blades at a tip Mach number of 0.9.

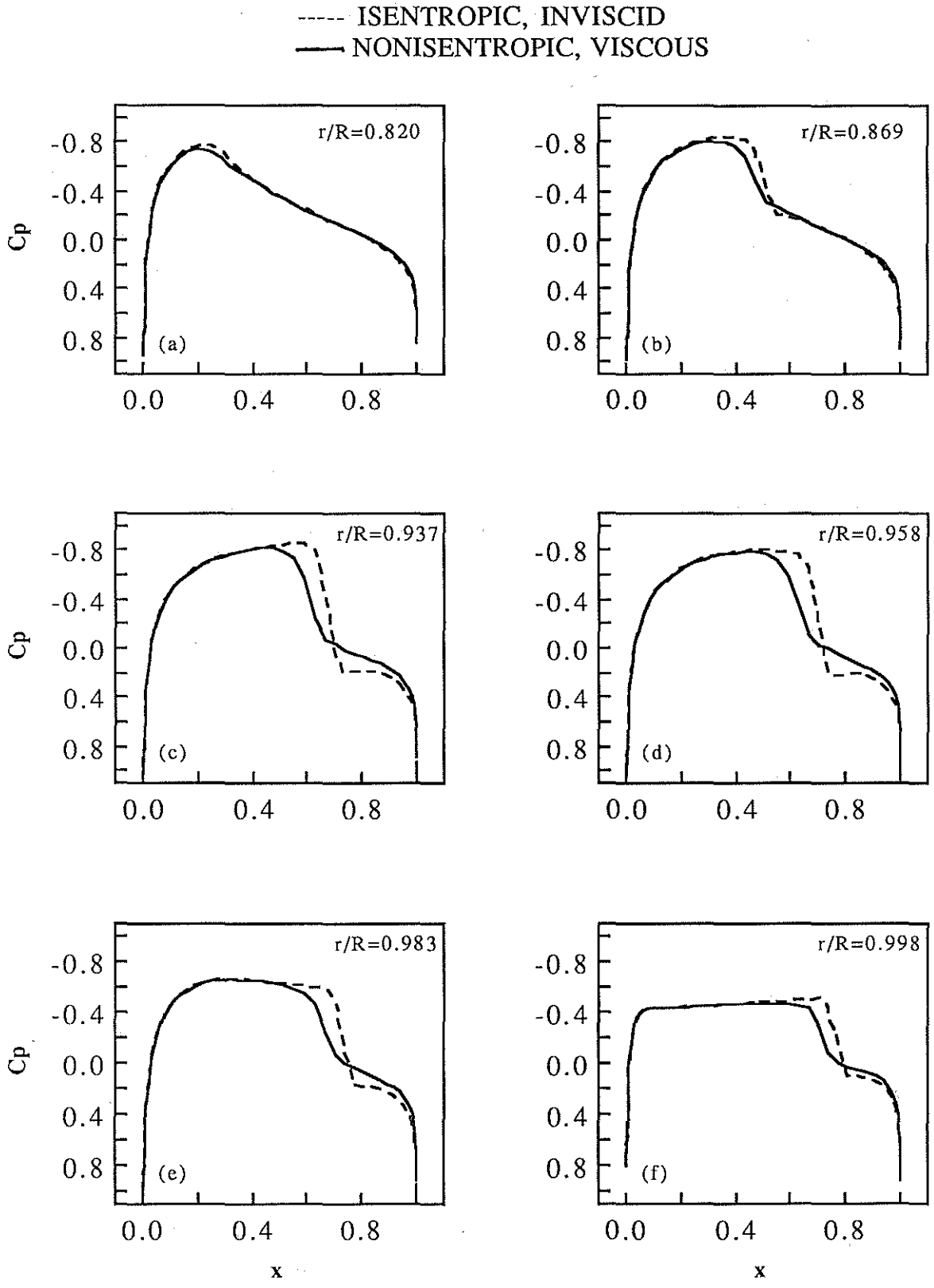

Fig. 11: Comparisons of pressure coefficients distribution with and without the viscous interaction for the hovering rotor with rectangular blades at a tip Mach number of 0.925.

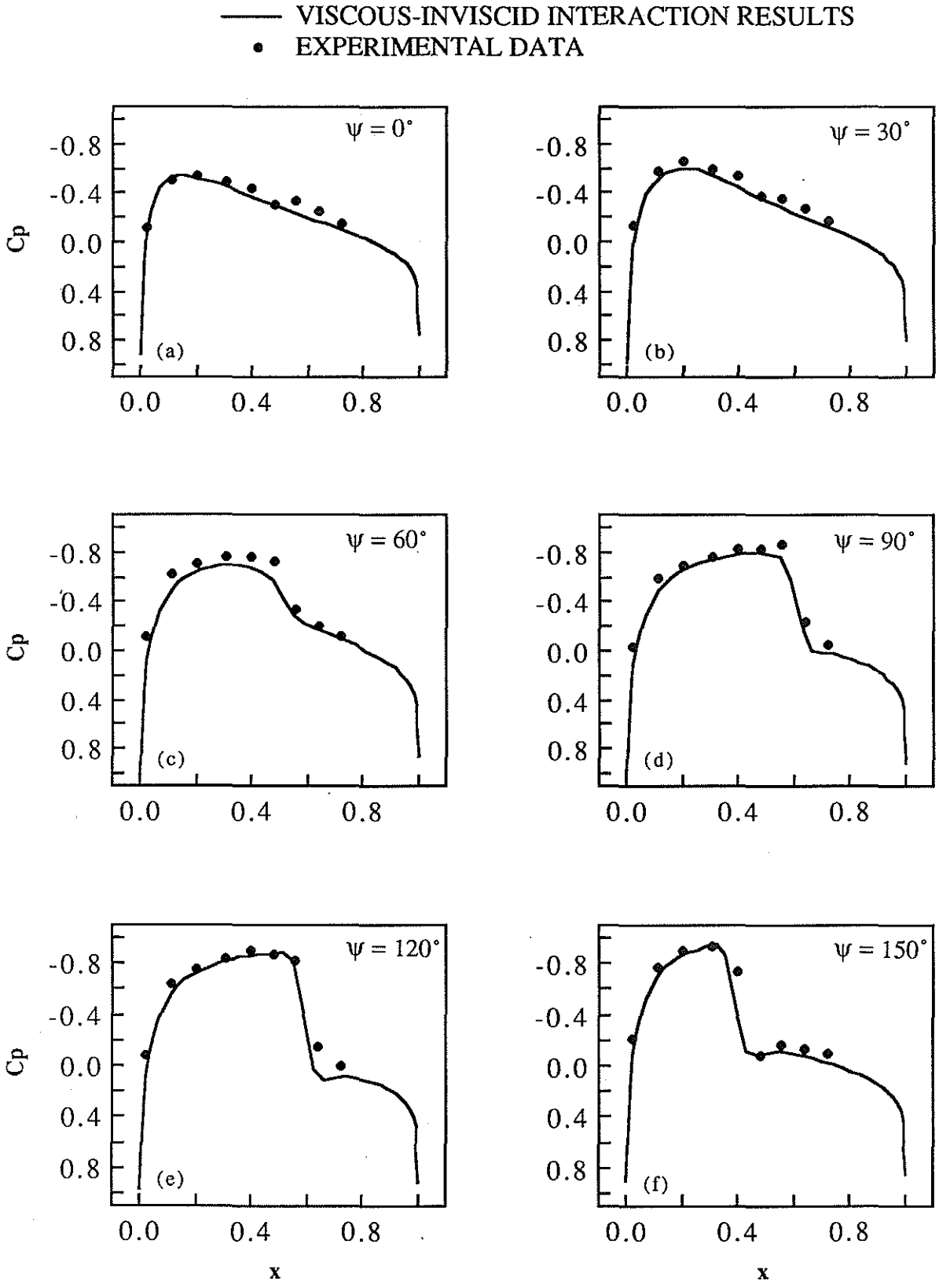

Fig. 12: Surface pressure results for a nonlifting rotor in forward flight, $M_T = 0.763$, AR=7.125, r/R=0.876, untwisted rectangular NACA 0012 blade.

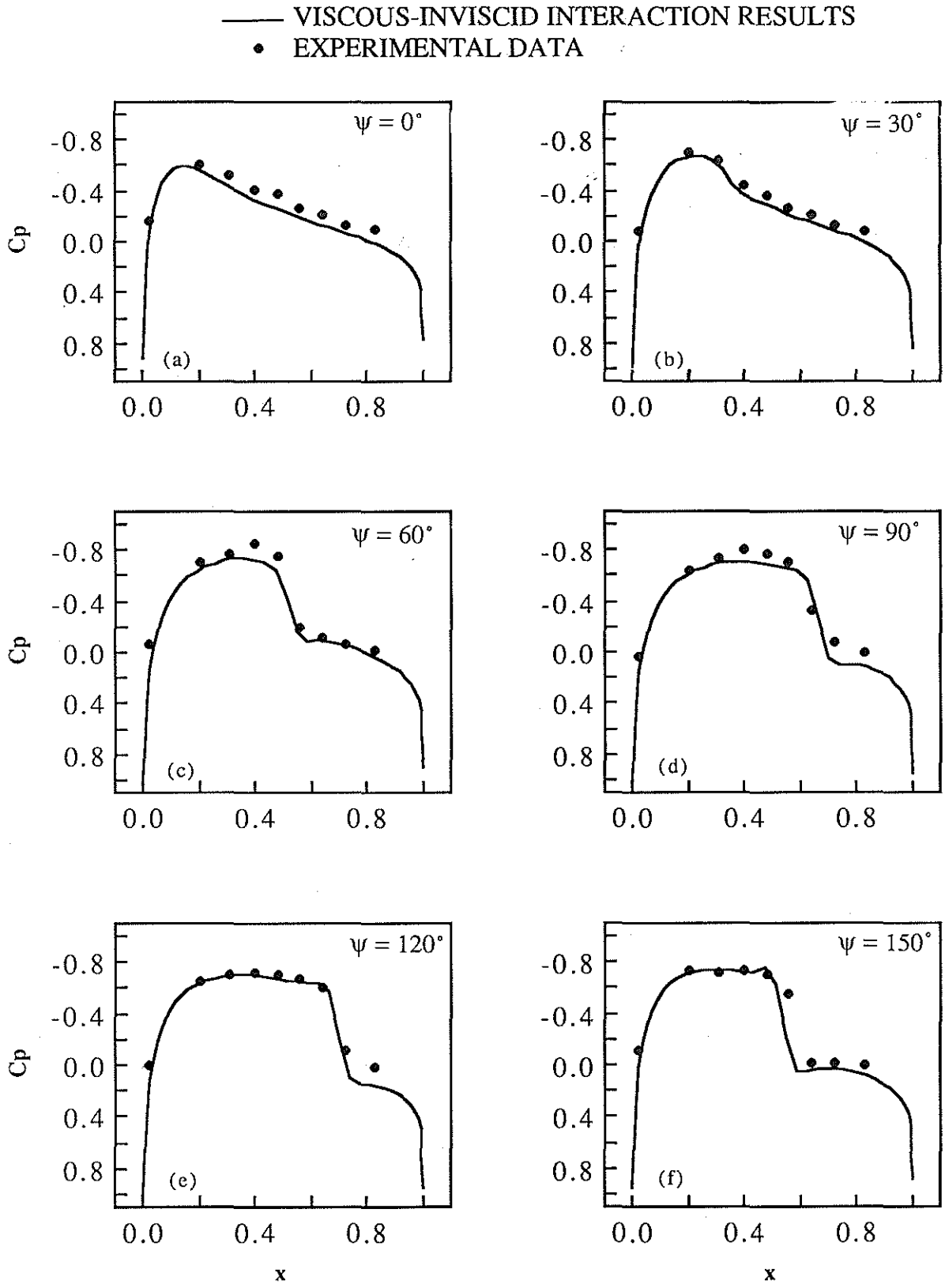

Fig. 13: Surface pressure results for a nonlifting rotor in forward flight, $M_T = 0.763$, AR=7.125, r/R=0.946, untwisted rectangular NACA 0012 blade.